Draft version April 10, 2017
Preprint typeset using LaTeX style emulateapj v. 12/16/11

arXiv:1704.02091v1 [astro-ph.HE] 7 Apr 2017

SUPERORBITAL MODULATION AT GEV ENERGIES IN THE γ-RAY BINARY LS I +61°303

Yi Xing, Zhongxiang Wang
Shanghai Astronomical Observatory, Chinese Academy of Sciences, 80 Nandan Road, Shanghai 200030, China

Jumpei Takata
Physics Department, Huazhong University of Science and Technology, Wuhan 430074, China
Draft version April 10, 2017

ABSTRACT

We report the results from our analysis of 8 years of the data for the γ-ray binary LS I +61°303, obtained with the Large Area Telescope onboard the *Fermi Gamma-Ray Space Telescope*. We find a significant dip around the binary's periastron in the superorbital light curves, and by fitting the light curves with a sinusoidal function, clear phase shifts are obtained. The superorbital modulation seen in the binary has been long known and different scenarios have been proposed. Based on our results, we suggest that the circumstellar disk around the Be companion of this binary has an elliptical shape and the major axis of the disk rotates at the superorbital period of 1667 days. As a result, the density of the ambient material around the compact star of the binary changes along the binary orbit over the superorbital period, causing the phase shifts in the modulation, and around periastron, the compact star probably enters the disk, causing the appearance of the dip. Numerical simulations may be conducted in order to study the detailed physical processes and verify our suggestion.

Subject headings: gamma rays:stars — stars:binaries — stars:individual (LS I +61°303)

1. INTRODUCTION

Galactic X-ray binaries consist of a neutron star or a black hole as the primary and a companion star. They are luminous X-ray sources in the sky powered by accretion with mass tranferred from the companion to the primary. In addition to the often-seen periodic signals related to their binary orbits, long-term, so-called superorbital periodic signals are also seen in a few of them. The origin of the superorbital flux variations is not clearly determined, but is thought to be due to the procession or warping of the accretion disk around a compact star (see Kotze & Charles 2012 for a brief review and references therein). Other proposed possible origins include X-ray state changes, the existence of precessing jets, or the existence of a tertiary star around a binary.

Having a Be star as the companion, LS I +61°303 is one of a handful high-mass X-ray binaries (HMXBs) that are γ-ray loud (see, e.g., Dubus 2013). Such γ-ray binaries are of great interests and have been under extensive studies, as complicated physical proecesses occur in them and produce remarkable phenomena at multiple wavelengths. The orbit of LS I +61°303 is elliptical with a period P_o of 26.496 days (Gregory 2002) and an eccetricity of $e \simeq 0.54$ (Aragona et al. 2009). Orbital flux or emission line variations have been detected at all wavelengths, from radio (e.g., Paredes et al. 1990; Marcote et al. 2016), optical (e.g., Grundstrom et al. 2007; Zamanov et al. 2014), X-ray (e.g., Paredes et al. 1997), to γ-ray GeV and TeV (e.g., Abdo et al. 2009; Albert et al. 2009). Very interestingly, a long-term 1667±8 days periodic signal (Gregory 2002) is also seen at nearly all the wavelengths (radio: Gregory 2002; Massi & Torricelli-Ciamponi 2016; optical: Zamanov & Martí 2000; X-ray: Chernyakova et al. 2012; Saha et al. 2016; GeV: Ackermann et al. 2013; TeV: Ahnen et al. 2016). Note that Massi & Torricelli-Ciamponi (2016) recently have determined a value of 1628±48 days for the long-term period.

How the superorbital varations are produced in LS I +61°303 is under debate. It has been thought that the variations are related to the cyclical changes in the mass loss of the Be companion or the density/size of the circumstellar disk around the companion (Zamanov et al. 1999). The interaction of the compact star (which is most likely a neutron star in this case; e.g., Papitto et al. 2012; Torres et al. 2012) with the disk is modulated, giving rise to the variations. Recently, arguing that the superorbital modulation is stable in the long-term radio data, Massi & Torricelli-Ciamponi (2014) have proposed a jet model, in which the jets from an accreting black hole precess at a period P_2 slightly longer than P_o, $P_2 \simeq 26.9$ days and the beat frequency corresponds to the superorbital signal.

In order to fully investigate the superorbital variations at γ-ray GeV energies and help understand the origin, we conducted detailed analysis of the data obtained with the Large Area Telescope (LAT) onboard the *Fermi Gamma-Ray Space Telescope (Fermi)* using the latest Pass 8 database. Previously Ackermann et al. (2013) have found sinusoidal variations, prominently seen during apastron orbital phases, at the superorbital period of 1667 days from the LAT data. Saha et al. (2016) recently have also obtained similar variations from their analysis of nearly 7-years LAT Pass 8 data. In addition to these results, our analysis indicates a significant dip around periastron and a clear phase-shift trend in the orbital-phase-resolved superorbital modulations. To explain the features, we suggest that the circumstellar disk around the companion would be eccentric and precess at the superorbital period. Here we report the results.

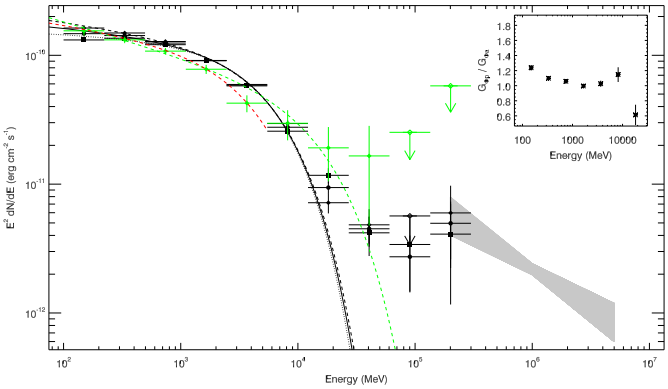

FIG. 1.— *Fermi* γ-ray spectra of LS I +61°303 during Φ_t (circles), Φ_p (diamonds) and Φ_a (squares). The black solid, dashed, and dotted lines are the 0.1–300 GeV exponentially cutoff power-law fits during Φ_t, Φ_p, and Φ_a, respectively. The grey area marks the power-law spectrum of LS I +61°303 obtained with VERITAS (Aliu et al. 2013), which was detected during the time intervals approximately within Φ_a. The ratios of the energy fluxes between Φ_p and Φ_a are plotted in the inner panel. The green data points are the fluxes obtained during the superorbital dip, and the green and red dashed lines are the exponentially cutoff power-law fits to the dip data at 0.1–300 and 0.1–5.5 GeV, respectively (see the text in Section 2.3.2).

2. DATA ANALYSIS AND RESULTS

2.1. *Fermi LAT Data*

LAT, onboard *Fermi*, is a γ-ray imaging instrument that scans the whole sky every three hours and can continuously observe thousands of GeV sources in the sky (Atwood et al. 2009). In this analysis, we selected 0.1–300 GeV LAT events from the *Fermi* Pass 8 database inside a $20^o \times 20^o$ region, which is centered at the position of LS I +61°303 given in the *Fermi* LAT third source catalog (Acero et al. 2015). The time period of the LAT data is 8 years from 2008-08-04 15:43:36 (UTC) to 2016-08-18 00:48:16 (UTC). Following the recommendations of the LAT team[1], we included events with zenith angles less than 90 degrees (preventing the Earth's limb contamination) and excluded the events with quality flags of 'bad'.

2.2. *Source's γ-ray Properties and Orbital Variability*

We first repeated the likelihood analysis and spectral analysis to the whole selected data, and confirmed the previously reported results obtained for this source (Abdo et al. 2009; Saha et al. 2016). In addition, we also repeated orbital variability analysis by folding the source's photons at the orbital period and obtaining the spectra during the periastron and apastron phase ranges.

2.2.1. *Likelihood analysis*

We included all sources within 20 degrees centered at the position of LS I +61°303 in the *Fermi* LAT 4-year catalog (Acero et al. 2015) to make the source model. The spectral forms of these sources are provided in the catalog. The spectral parameters of the sources within 5 degrees from LS I +61°303 were set as free parameters, and the other parameters were fixed at their catalog values. LS I +61°303 was included in the source model as a point source with emission modelled with an exponentially cutoff power law, $dN/dE = N_0 E^{-\Gamma} \exp[-(E/E_c)]$, where Γ and E_c are the photon index and cutoff energy, respectively. In addition, the background Galactic and extragalactic diffuse emission was included, with the spectral model gll_iem_v06.fits and the file iso_P8R2_SOURCE_V6_v06.txt, respectively, used in the source model. The normalizations of the diffuse components were set as free parameters.

Using the LAT science tools software package `v10r0p5`, we performed standard binned likelihood analysis to the LAT data in the 0.1–300 GeV band. The Instrument Response Functions (IRFs) of P8R2_SOURCE_V6 were used. The γ-ray emission of LS I +61°303 during the total data set (Φ_t) was detected to have a Test Statistic (TS) value of 136681, and $\Gamma = 2.086 \pm 0.009$ and $E_c = 5.5 \pm 0.2$ were obtained. For comparison, we also repeated the likelihood analysis with emission from LS I +61°303 modelled with a simple power law $dN/dE = N_0 E^{-\Gamma}$, and obtained $\Gamma = 2.314 \pm 0.004$ with a TS value of 140997. We estimated the significance of the spectral cutoff from $\sqrt{-2\log(L_{pl}/L_{exp})}$, where L_{exp} and L_{pl} are the maximum likelihood values for the power law model with and without the cutoff respectively (Abdo et al. 2013). The spectral cutoff was detected at a significance of 38σ. The parameters of the exponentially cutoff power-law fit are listed in Table 1.

2.2.2. *Spectral Analysis*

We extracted the γ-ray spectrum of LS I +61°303 by performing maximum likelihood analysis of the LAT data in 10 evenly divided energy bands in logarithm from 0.1–300 GeV. In the extraction, the spectral normalizations of the sources within 5 degrees from LS I +61°303 were set as free parameters, while all the other parameters of the sources were fixed at the values obtained from the above maximum likelihood analysis. We kept only spectral data points when TS greater than 9 ($>3\sigma$ significance) and derived 95% flux upper limits otherwise. The obtained spectrum is shown in Figure 1, with the flux values of the spectral data points provided in Table 2.

2.2.3. *Orbital variability analysis*

We performed timing analysis to the 0.1–300 GeV LAT data of LS I +61°303 to study the orbital variations of the source. We selected γ-ray photons within an aperture radius of 2 degrees from LS I +61°303, as most of the sources in the source model are located >2 degrees away from LS I +61°303, and weighted them by their probabilities of originating from the binary (calculated with *gtsrcprob* in the science tools software package) using the fitted source model obtained in Section 2.2.1. Orbital phases ϕ_o for the photons were assigned using the ephemeris given in Aragona et al. (2009). We folded the weighted photons into 16 orbital phase bins, and plotted them over the exposures (calculated with *gtexposure*) in each of the bins in Figure 2. The folded light curve has modulation peak approximately at the periastron (ϕ_o of 0.275), consistent with that in the previous studies (Abdo et al. 2009; Hadasch et al. 2012).

We further defined the orbital phase ranges of 0.0–0.5 around periastron and 0.5–1.0 around apastron as Φ_p and Φ_a, respectively, and performed likelihood analysis and

[1] http://fermi.gsfc.nasa.gov/ssc/data/analysis/scitools/

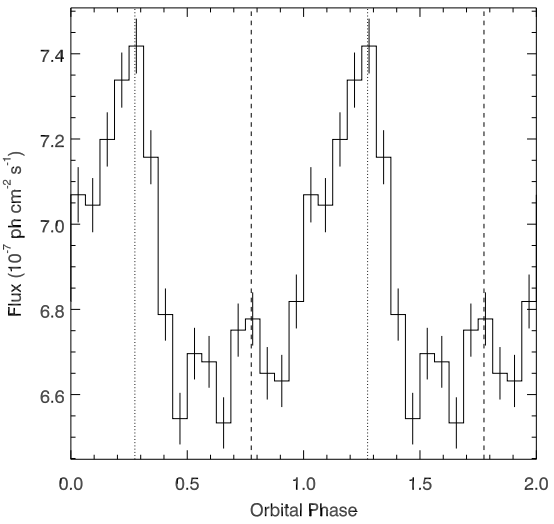

FIG. 2.— Orbital light curve of LS I +61°303, where the dotted and dashed lines mark the phases of the periastron and apastron, respectively. For clarity, two cycles are displayed.

spectral analysis to the LAT data during these two phase ranges. The likelihood results are given in Table 1. The spectra are plotted in Figure 1, with the spectral flux values listed in Table 2. The Γ value during Φ_p is $>6\sigma$ higher than that during Φ_a (see Table 1), indicating a softer γ-ray emission during the former than the latter. The E_c value during the two phase ranges are consistent within uncertainties. In order to show the detailed differences between the emission from the two phase ranges, we compared their ratios of the energy fluxes (the inner panel of Figure 1, where only the ratios in the energy ranges of <27.2 GeV are shown as the flux uncertainties in the energy ranges of 27.2–60.5 and 134.7–300 GeV are too large to be reliable). As can be seen, the γ-ray emission during the former is higher than that during the latter in the low energy ranges, and the ratio decreases to $\simeq 1$ in the middle energies, and in the high energy range of 12.2–27.2 GeV the γ-ray emission during the former is lower than that during the latter. This comparison helps indicate the spectral changes between the two phase ranges found from the likelihood analysis.

2.3. *Superorbital Variability Analysis*

2.3.1. *Orbitally-resolved superorbital variability*

From previous work (Ackermann et al. 2013; Saha et al. 2016), it has been shown that the shape of superorbital modulation depends on orbital phase. We therefore performed the same superorbital analysis. γ-ray photons in the 0.1–300 GeV within an aperture radius of 2 degrees from LS I +61°303 were selected and weighted by their probabilities of originating from the source using the source model obtained in Section 2.2.1. Superorbital phases ϕ_{so} for the photons were assigned using the ephemeris given in Gregory (2002). We note that the superorbital period in Gregory (2002) is consistent with that found by Massi & Torricelli-Ciamponi (2016) within the uncertainties. In addition the period difference is only $\sim$0.02 in phase (which is small compared to the 10 superorbital phase bins we used in the following analysis and did not affect our results). We folded the weighted photons into 10 superorbital phase bins, while the same as that in Ackermann et al. (2013), the photons in 10 orbital phase ranges (0.0–0.1, ..., 0.9–1.0) were separatedly considered.

The 10 light curves, divided by the exposures (calculated with *gtexposure*), are shown in Figure 3. As can be seen, the superorbital modulations were significant during the five orbital phase ranges near apastron: the χ^2-test values are 131–386 for 9 degrees of freedom (dof; a value of 22 corresponds to a 99% confidence level for variations). During the other five orbital ranges near periastron, the modulations are relatively weak (the χ^2-test values are 32–165 for 9 dof), but with a significant dip appearing at ϕ_{so}= 0.65 in the orbtial ranges of 0.1–0.5. Excluding the dip point, we checked the χ^2-test values again for the four light curves, χ^2 =30–70 for 8 dof (a value of 20 corresponds to the 99% confidence level), indicating that the superorbital modulations were still significant.

Most of the light curves appear to have a sinusoidal-like shape, and thus following the previous work in Ackermann et al. (2013) and Saha et al. (2016), we fit them with a sinusoidal function $A[1+\sin(2\pi(\phi_{so} - \phi_{so,peak})+\pi/2)]/2+C$, where $\phi_{so,peak}$ is the superorbital peak phase, and A and C are the modulation amplitude and constant flux (in units of photon cm^{-2} s^{-1}), respectively. For the four light curves near periastron that have the dip, the dip data point was not included in the fitting. The resulting reduced χ^2 values were in a range of $\sim$0.6–13, suggesting that either most of the light curves are not exactly sinusoidal or the uncertainties on the data points were under-estimated. In any case, we added an artificial value in quadrature with the uncertainties to lower the reduced χ^2 values to $\sim$1. The obtained best fits are plotted as dotted lines in Figure 3, and the fit results are given in Table 3. We also evaluated the significance of the dip by comparing the observed and best-fit model fluxes at ϕ_{so} = 0.65, which are also listed in Table 3. The dip was indeed significant during the orbital phase ranges of 0.1–0.5 ($\simeq$3–7σ). During the other six orbital phase ranges, the dip was not significantly detected.

As pointed above, the superorbital modulation amplitudes near apastron are obviously larger than those near periastron. We show the best-fit parameters of the sinusoidal functions in Figure 4, and the results confirm it quantatively: the relative amplitudes (A/C) are approximately between 9%–16% during ϕ_o = 0.0-0.5 and 27%–50% during ϕ_o = 0.5–1.0. On the other hand, the constant fluxes near periastron are approximately 20% higher than those near apastron. In addition, a striking feature is that the superorbital modulation peak shifts with orbital phase, from $\phi_{so} \simeq 0.1$ at ϕ_o = 0.55 to $\phi_{so} \simeq 1.0$ at $\phi_o = 1.45$ (see the bottom panel of Figure 4). This feature was noted by Ackermann et al. (2013) and Saha et al. (2016), but our analysis shows that there is a consistent pattern for the shifts over the whole superorbital/orbital phase.

2.3.2. *Properties of the dip*

We investigated the dip's properties by first determining the orbital phase range in which the dip is the most significant. We searched through different range values by repeating the above sinusoidal fitting process, and found that in the 0.3 orbital phase range centered at ϕ_o=0.285, the dip was detected at the highest signifi-

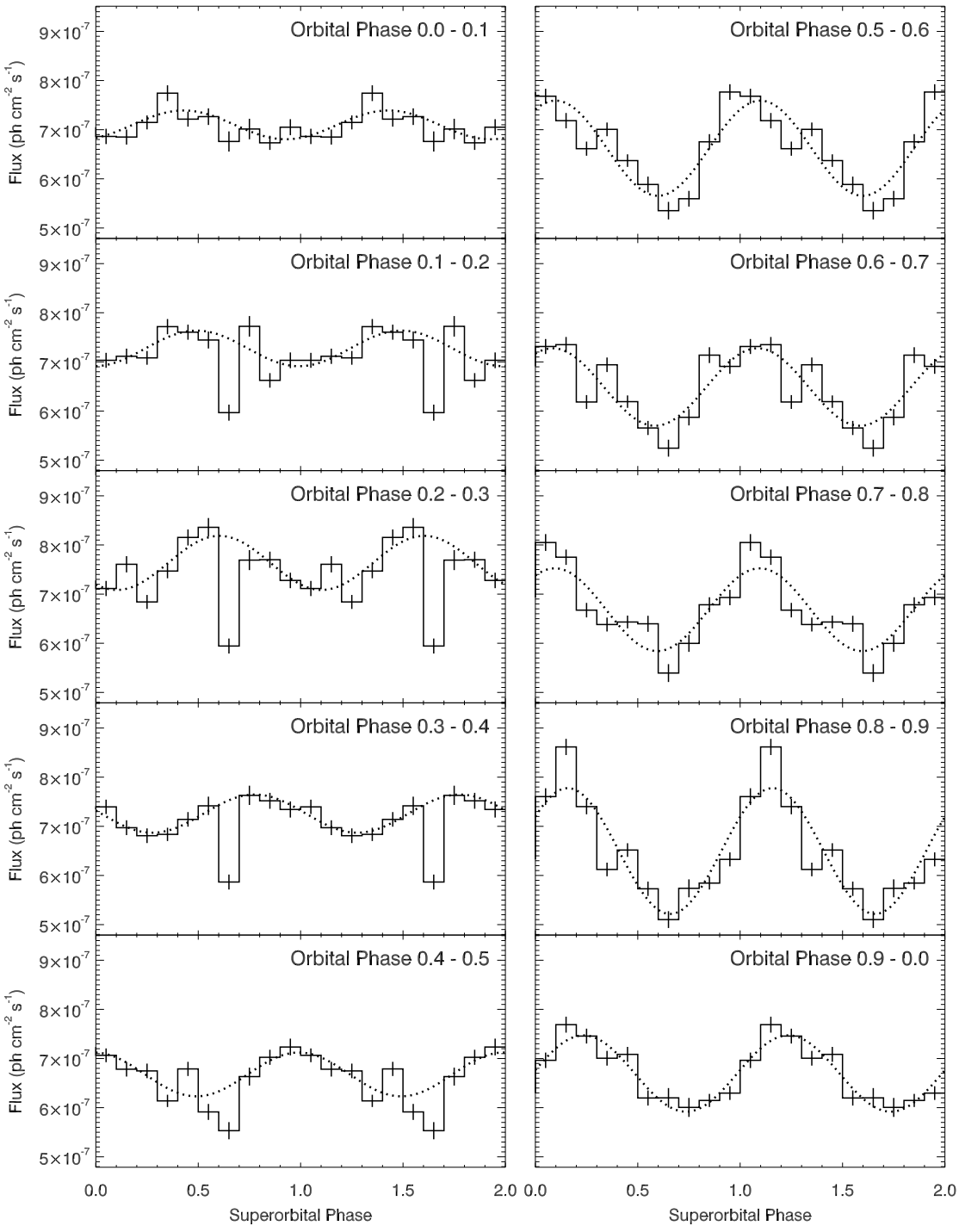

FIG. 3.— 0.1–300 GeV superorbital light curves in 10 orbital phase ranges, with the best-fit sinusoidal functions (Table 3) plotted as dotted lines. Two cycles are displayed for clarity.

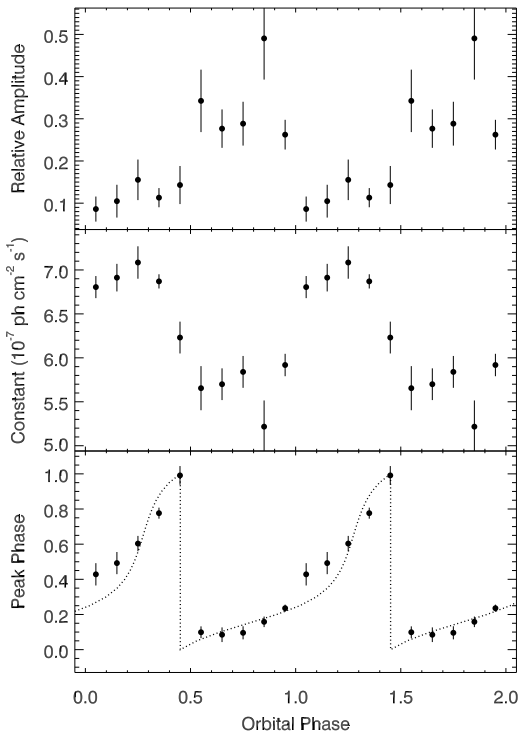

FIG. 4.— Parameters of the best-fit sinusoidal functions for the superorbital light curves in each of the 10 orbital phase ranges. Two cycles are displayed for clarity. The dotted line in the bottom panel is the model curve obtained by considering a precessing eccentric disk around the Be companion (see the text in § 3).

cance of 10σ (after adding an artificial value to the uncertainties to have a reduced $\chi^2 \simeq 1$). We also checked its dependence on energy. Analyzing light curves in different energy ranges, we found that the dip exists only significantly in the energy range of <5.5 GeV. The superorbital light curves in the energy ranges of below and above 5.5 GeV are shown in the left panels of Figure 5. In the >5.5 GeV energy range, the light curve was nearly a constant, as the χ^2 test value was only 12.1 (for 9 dof). As a comparison, the 0.3 phase range light curves around the apastron were also shown in the right panels of the figure. For the >5.5 GeV one, modulation is still visible, with a χ^2 test value of 21.1 (for 9 dof; at a 98.8% confidence level).

We also performed analysis to the data during the dip Φ_d determined above (i.e., $\phi_o = 0.135$–0.435 and $\phi_{so} = 0.6$–0.7), in order to check if there are any physical differences between the dip and the other phase ranges. The likelihood results are given in Table 1, and the obtained spectrum is shown in Figure 1, with the spectral flux values listed in Table 2. The photon index, $\Gamma = 2.27 \pm 0.02$, is significantly higher than those obtained from the total data or periastron/apastron orbital phase ranges and the cutoff energy, $E_c = 16 \pm 4$ GeV, is also higher but with the very large uncertainty. Examining the dip spectrum in Figure 1, the spectral data points may not be well described by the exponentially cutoff power-law fit, as the fit has a higher tail (resulting the high cutoff energy of 16 GeV). Since the dip is only significant in the <5.5 GeV data, we tested to limit the likelihood analysis to the 0.1–5.5 GeV data and found that

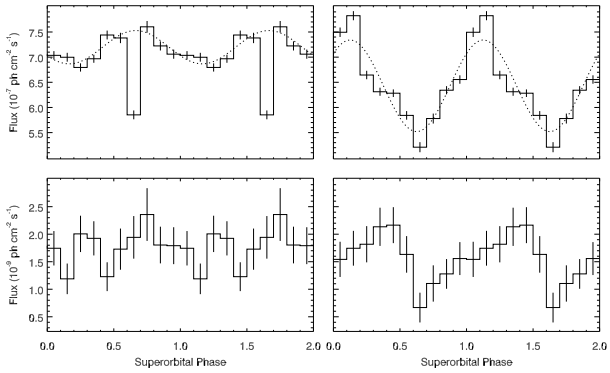

FIG. 5.— Superorbital light curves in ≤5.5 (*upper*) and >5.5 GeV (*bottom*) bands during $\phi_o = 0.135$–0.435 (*left* panels). The corresponding light curves during $\phi_o = 0.625$–0.925 are shown in the *right* panels. The best-fit sinusoidal functions to the light curves in the upper panels are plotted as dotted lines. Two cycles are displayed for clarity.

the fit results, $\Gamma = 2.15 \pm 0.03$ and $E_c = 4.2 \pm 0.5$ GeV (see also Table 1) are then consistent. Therefore there is no clear evidence for having a different spectrum during the dip.

3. DISCUSSION

At *Fermi* LAT energies, γ-ray emission from LS I +61°303 obviously have two components, one described by a power law with an exponential cutoff at ~ 5 GeV and one slightly rising from ~ 27 GeV to 200 GeV. The former and the latter can be connected to the emission at MeV/KeV and TeV energies respectively (e.g., Zdziarski et al. 2010). No matter whether the primary is a pulsar or a black hole with jets, the former is likely due to synchrotron radiation and the latter due to the inverse Compton (IC) scattering (e.g., Zdziarski et al. 2010; Saha et al. 2016). This spectral feature is similar to that in the high-mass pulsar binary PSR B1259−63/LS 2883 (e.g., Xing et al. 2016), the only γ-ray binary with a known primary, although the synchrotron tail of the latter source approximately ends at ~ 1 GeV. (We note that in either pulsar or black hole accretion models such as those in Zdziarski et al. (2010) or Jaron et al. (2016), respectively, GeV emission can come from the IC scattering processes, but then the TeV component remains to be explained.)

Based on the above general scenario for emission from LS I +61°303, our analysis has shown that in addition to be orbitally modulated, the synchrotron component is also superorbitally modulated, particularly by showing a dip (only significantly seen at < 5.5 GeV energy range; cf., Figure 5) around periastron. Although the modulations at different orbital phases may not be well described by a simple sinusoid used in our analysis, the general properties we have obtained should not be affected. Near periastron, the average flux is high and the modulation amplitude is low, and near apastron, we see the opposite (Figure 4). The sinusoidal-like modulation feature has been pointed out by the previous studies (Ackermann et al. 2013; Saha et al. 2016), but our analysis confirms its existence over the whole orbital phase ranges.

In order to explain the dip and phase shifts in the superorbital light curves (as a function of orbital phase),

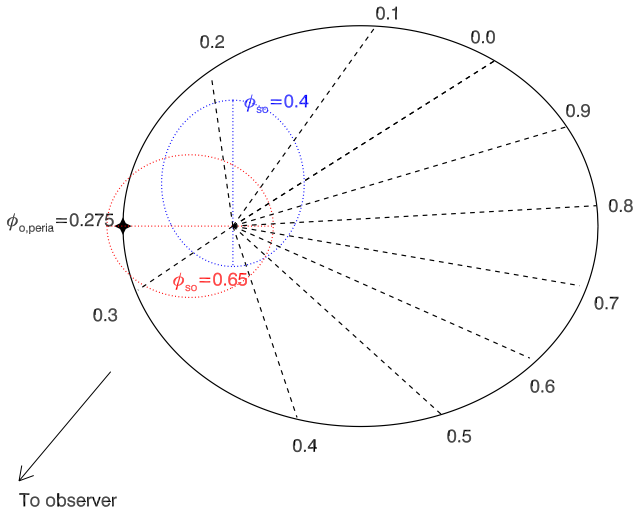

FIG. 6.— Schemetic diagram for an eccentric circumstellar disk around the Be companion in the binary, where the semi-minor axis b is set to be the averaged value of 26.5 $R_\odot$ obtained for the disk, and the semi-major axis a be (26.5+4.4) $R_\odot$ (4.4 $R_\odot$ is the 1σ uncertainty; see Zamanov et al. 2013). We define when the major axis of the disk points to the periastron of the binary, the superorbital phase $\phi_{so} = 0.65$.

we suggest that they indicate an eccentric circumstellar disk around the companion. In Figure 6, we show a schemetic diagram for this scenario. Long-term optical spectroscopy has clearly shown that the disk has size changes at the superorbital period (Zamanov & Martí 2000; Zamanov et al. 2013). It is possible that in addition to the changes in radius of the disk, the disk might have an elliptical shape and the major axis of the disk would rotate at the superorbital period of 1667 days. At $\phi_{so} = 0.6$–0.7, the disk extends over the periastron substantially, causing the compact star to be totally inside the disk. The synchrotron emission is thus significantly reduced (due to blocking/scattering) or even quenched (due to state changes; see Torres et al. 2012), forming the dip. We note that recently, Zamanov et al. (2016) have concluded that the compact star passes through the outer part of the disk at periastron from their optical spectrosopic study of the binary.

Since around periastron, the overall flux is high, particularly in <1 GeV low-energy range (Figure 1), it is reasonable to assume that the synchrotron component is somehow related to the high density condition to the compact star. Therefore the superorbital modulation peak probably corresponds to the condition of being surrounded by the ambient matter with the highest density, the location of which would slowly move along the binary orbit due to the precession of the eccentric disk. Indeed, if we assume that the major axis of the disk crosses periastron when $\phi_{so} = 0.65$ (Figure 6) and the direction of the major axis of the disk points to the orbital location of the highest ambient density, we can obtain the dashed curve shown in Figure 4, which approximately explains the phase shifts seen in the superorbital light curves.

The suggested explanation for the superorbital features probably favors the pulsar scenario for LS I +61°303 and should be further investigated by numerical simulations. For example, it has been considered that a young neutron star is the compact star in LS I +61°303 and the neutron star can switch between the states of being a propeller (when around periastron) and rotationally powered (when around apastron; Papitto et al. 2012; Torres et al. 2012). If we consider superorbitally-modulated condition changes along the binary orbit, whether this scenario can reproduce the dip and the superorbital modulations at different orbital phase ranges can be studied. Questions, such as if the dip is due to the sudden turn-off of the emission from the neutron star near periastron and if the amplitdue changes (low near periastron and high near apastron) are related to state changes, may be answered. Spectral changes in emission from the orbital phase around periastron and apastron are seen in our orbital variability analysis (cf., Section 2.2.3), which may be evidence for the state changes. Finally we point out that any long-term process that can cause the condition changes along the orbit might explain the superorbital phase shifts as a function of orbital phase. For example, if the rotation axis of the Be star has an angle to that of the orbital plane, and if it precesses at the superorbital period, an anisotropic poloidal wind (e.g., Papitto et al. 2012) may be able to cause density changes along the orbit over the superorbital period as well.

This research made use of the High Performance Computing Resource in the Core Facility for Advanced Research Computing at Shanghai Astronomical Observatory. This research was supported by the National Program on Key Research and Development Project (Grant No. 2016YFA0400804) and the National Natural Science Foundation of China (11373055, 11633007). Z.W. acknowledges the support by the CAS/SAFEA International Partnership Program for Creative Research Teams. JT is supported by NSFC grants of Chinese Government under 11573010 and U1631103.

REFERENCES

Abdo, A. A., Ackermann, M., Ajello, M., et al. 2009, ApJ, 701, L123
Abdo, A. A., Ajello, M., Allafort, A., et al. 2013, ApJS, 208, 17
Acero, F., Ackermann, M., Ajello, M., et al. 2015, ApJS, 218, 23
Ackermann, M., Ajello, M., Allafort, A., et al. 2013, ApJS, 209, 34
Ahnen, M. L., Ansoldi, S., Antonelli, L. A., et al. 2016, A&A, 591, A76
Albert, J., Aliu, E., Anderhub, H., et al. 2009, ApJ, 693, 303
Aliu, E., Archambault, S., Behera, B., et al. 2013, ApJ, 779, 88
Aragona, C., McSwain, M. V., Grundstrom, E. D., et al. 2009, ApJ, 698, 514
Atwood, W. B., Abdo, A. A., Ackermann, M., et al. 2009, ApJ, 697, 1071
Chernyakova, M., Neronov, A., Molkov, S., et al. 2012, ApJ, 747, L29
Dubus, G. 2013, A&A Rev., 21, 64
Gregory, P. C. 2002, ApJ, 575, 427
Grundstrom, E. D., Caballero-Nieves, S. M., Gies, D. R., et al. 2007, ApJ, 656, 437
Hadasch, D., Torres, D. F., Tanaka, T., et al. 2012, ApJ, 749, 54
Jaron, F., Torricelli-Ciamponi, G., & Massi, M. 2016, A&A, 595, A92
Kotze, M. M., & Charles, P. A. 2012, MNRAS, 420, 1575

Marcote, B., Ribó, M., Paredes, J. M., et al. 2016, MNRAS, 456, 1791
Massi, M., & Torricelli-Ciamponi, G. 2014, A&A, 564, A23
—. 2016, A&A, 585, A123
Papitto, A., Torres, D. F., & Rea, N. 2012, ApJ, 756, 188
Paredes, J. M., Estalella, R., & Rius, A. 1990, A&A, 232, 377
Paredes, J. M., Marti, J., Peracaula, M., & Ribo, M. 1997, A&A, 320, L25
Saha, L., Chitnis, V. R., Shukla, A., Rao, A. R., & Acharya, B. S. 2016, ApJ, 823, 134
Torres, D. F., Rea, N., Esposito, P., et al. 2012, ApJ, 744, 106
Xing, Y., Wang, Z., & Takata, J. 2016, ApJ, 828, 61
Zamanov, R., & Martí, J. 2000, A&A, 358, L55
Zamanov, R., Martí, J., Stoyanov, K., Borissova, A., & Tomov, N. A. 2014, A&A, 561, L2
Zamanov, R., Stoyanov, K., Martí, J., et al. 2013, A&A, 559, A87
Zamanov, R. K., Martí, J., Paredes, J. M., et al. 1999, A&A, 351, 543
Zamanov, R. K., Stoyanov, K. A., Martí, J., et al. 2016, A&A, 593, A97
Zdziarski, A. A., Neronov, A., & Chernyakova, M. 2010, MNRAS, 403, 1873

TABLE 1
EXPONENTIALLY CUTOFF POWER-LAW FITS FOR LS I +61°303.

Data set	>0.1 GeV Flux (10^{-7} photon cm^{-2} s^{-1})	Γ	E_c (GeV)	TS
Total data (Φ_t)	8.79±0.07	2.086±0.009	5.5±0.2	136681
Periastron (Φ_p)	9.5±0.1	2.13±0.01	5.9±0.3	73272
Dip (Φ_d)	8.8±0.3	2.27±0.02	16±4	3190
Dip (Φ_d, <5.5 GeV)	8.7±0.3	2.15±0.03	4.2±0.5	3080
Apastron (Φ_a)	8.13±0.09	2.04±0.01	5.1±0.3	63691

TABLE 2
Fermi LAT FLUX MEASUREMENTS OF LS I +61°303.

Band (GeV) \ Data set	Total data (Φ_t)	Periastron (Φ_p)	Dip (Φ_d)	Apastron (Φ_a)
0.1–0.2	14.7±0.2	16.3±0.2	15±1	13.2±0.3
0.2–0.5	14.2±0.1	14.9±0.2	13.2±0.8	13.6±0.2
0.5–1.1	12.4±0.1	12.8±0.2	10.8±0.6	12.1±0.1
1.1–2.5	9.1±0.1	9.1±0.2	7.8±0.6	9.1±0.2
2.5–5.5	5.9±0.1	5.9±0.2	4.3±0.6	5.8±0.2
5.5–12.2	2.8±0.1	3.0±0.2	3.0±0.8	2.6±0.2
12.2–27.2	0.9±0.1	0.7±0.1	1.9±0.9	1.2±0.2
27.2–60.5	0.5±0.1	0.5±0.2	2±1	0.4±0.1
60.5–134.7	0.3±0.1	0.6	2.5	0.3±0.2
134.7–300	0.5±0.2	0.6±0.4	5.8	0.4±0.3

Fluxes are calculated from $E^2dN(E)/dE$ and in units of 10^{-11} erg cm^{-2} s^{-1}, while those values without uncertainties are the 95% upper limits.

TABLE 3
SINUSOIDAL FITS FOR THE ORBITALLY-RESOLVED SUPERORBITAL LIGHT CURVES OF LS I +61°303.

Orbital phase	$A/10^{-7}$ (photon cm^{-2} s^{-1})	$C/10^{-7}$ (photon cm^{-2} s^{-1})	$\phi_{so,peak}$	Significance of the dip (σ)
0.0–0.1	0.6±0.2	6.8±0.1	0.43±0.06	1.3
0.1–0.2	0.7±0.3	6.9±0.2	0.49±0.06	4.5
0.2–0.3	1.1±0.3	7.1±0.2	0.60±0.04	5.4
0.3–0.4	0.8±0.2	6.87±0.08	0.78±0.03	7.4
0.4–0.5	0.9±0.3	6.2±0.2	0.99±0.05	3.1
0.5–0.6	1.9±0.4	5.7±0.3	0.10±0.03	1.2
0.6–0.7	1.6±0.3	5.7±0.2	0.08±0.04	2.0
0.7–0.8	1.7±0.3	5.8±0.2	0.10±0.04	1.9
0.8–0.9	2.6±0.5	5.2±0.3	0.16±0.03	0.4
0.9–0.0	1.6±0.2	5.9±0.1	0.24±0.02	0.7